Comm. Math. Sci.
Vol. 2, No. 4, pp. 535–552

COMPUTATION OF A MOVING DROP/BUBBLE ON A SOLID SURFACE USING A FRONT-TRACKING METHOD *

HUAXIONG HUANG †, DONG LIANG ‡, AND BRIAN WETTON §

Abstract. In this paper we outline a front-tracking method for computing the moving contact line. In particular, we are interested in the motion of two-dimensional drops and bubbles on a partially wetting surface exposed to shear flows. Peskin's Immersed Boundary Method is used to model the liquid-gas interface, similar to the approach used by Unverdi and Traggvason. The movement near the moving contact line is modelled by a slip condition, the value of the dynamic contact angle is determined by a linear model, and the local forces are introduced at the moving contact lines based on a relationship of moving contact angle and contact line speed. Numerical examples show that the method can be applied to the motion of drops and bubbles on a solid surface over a wide range of parameter values.

Key words. Moving drop on surface, moving contact line, dynamic contact angle, and numerical computation.

1. Problem Description

The motion of a drop on a solid surface has been a subject of extensive research since 1970s not only because of its relevance to many industrial and engineering applications, but also due to the complication caused by the moving contact line. In this paper we consider a two dimensional liquid drop (or a gas bubble) with a given volume V resting on a flat solid surface with the fluid outside the drop also at rest initially. At time $t>0$, the outside fluid (air) starts moving, driven by a shear flow parallel to the flat surface. The objective of the study is to develop a numerical method which can be used to investigate the behaviour of moving drops and bubbles on a solid surface under the influence of flow conditions of the external fluid and the wetting properties of the flat solid surface.

Most of the existing work considers thin drops so that the lubrication theory can be applied, cf. [4, 5, 7, 10] and references therein. In the limit of creeping flows, a boundary integral method can be used, see for example [1]. A combination of the Levelset method and the immersed interface method has been used in [9] to study the reactive spreading of thin drops on a solid surface based on lubrication theory approximation. However, for a fat drop immersed in flows with finite Reynolds numbers, the full Navier-Stokes equations have to be used. In this paper, we extend the method in [21] to compute the motion of liquid drops (and bubbles) on a solid surface with moving contact lines. The main challenge, in addition to capturing the moving interface between the liquid and gas phases, is to incorporate conditions at the moving contact lines. The method developed in [21] is based on the immersed boundary method, originally developed by Peskin for simulating blood flows in the heart [12]. One of the main advantages of the immersed boundary formulation is its ease for implementation even though Peskin's original formulation is not as accurate as the more recent immersed interface method developed by LeVeque and Li [11].

---

*Received: April 6, 2004; accepted (in revised version): September 21, 2004. Communicated by Tao Tang.

†Department of Mathematics and Statistics, York University, Toronto, Ontario, Canada M3J 1P3 (hhuang@yorku.ca).

‡Department of Mathematics and Statistics, York University, Toronto, Ontario, Canada M3J 1P3 (dliang@yorku.ca).

§Department of Mathematics, University of British Columbia, Vancouver, B.C., Canada V6T 1Z2 (wetton@math.ubc.ca).

To simplify the problem, we consider a rectangular domain $\Omega = (0:1)\times(0:1)$. The left boundary is a solid surface with a drop resting in the middle initially. The right boundary is either a slip-free surface or a no-slip wall with a given velocity. In-flow conditions are given at the bottom boundary and the outflow conditions are applied at the top boundary. An alternative setup is to impose a periodic condition at the bottom and top boundaries. The liquid-gas interface is modelled by the front-tracking method [21]. The movement along the solid boundary is modelled by a slip condition [3, 8], the dynamic contact angle is based on a linear model in [2, 4], and a local force is introduced at the moving contact lines based on a relationship of the moving contact angle and the contact line speed. In addition, we use cubic splines to fit the interface so that it maintains high accuracy of both interface and the its curvature. Numerical examples and grid refinement tests show that the method can be applied to the motion of drops and bubbles on a solid surface over a wide range of parameter values.

The rest of this paper is organized as follows. In Section 2, we describe the detailed mathematical model. Numerical method and implementation are discussed in Section 3. Numerical experiments are given in Section 4, followed by a short summary and a discussion of future work in Section 5.

2. Mathematical Model

We assume that the motion of the fluids is governed by the Navier-Stokes equations

$$\frac{\partial \rho\vec{v}}{\partial t} + \nabla\cdot(\rho\vec{v}\vec{v}) = -\nabla p + \vec{g} + \nabla\cdot(2\mu D), \tag{2.1}$$

where $\vec{v}$ is the velocity vector, p the pressure, $\vec{g}$ the gravity, $2\mu D$ the stress tensor and $D = \nabla\vec{v} + \nabla^T\vec{v}$, μ the viscosity, and ρ the density. The equations are valid both inside and outside the drop except at the interface. Furthermore, we assume that the viscosity and density are constants for each fluid and that the fluids are incompressible

$$\nabla\cdot\vec{v} = 0. \tag{2.2}$$

The interface Γ between liquid and gas is a free boundary where the following conditions hold

$$\begin{aligned} [2\mu D\cdot\vec{\tau}]_\Gamma &= 0, \\ [-p\vec{n} + 2\mu D\cdot\vec{n}]_\Gamma &= \sigma\kappa\vec{n}, \\ \frac{d\vec{X}}{dt} &= \vec{v}\left(\vec{X},t\right), \ on\ \Gamma, \end{aligned} \tag{2.3}$$

where $[\ \cdot\ ]_\Gamma$ denotes the jump of the values at the interface Γ, $\vec{n}$ and $\vec{\tau}$ are the unit vectors in the normal and tangential directions, respectively, σ is the surface tension coefficient between liquid-gas, κ is the curvature of the interface, and $\vec{X}$ is the position vector of the interface. The first two equations in (2.3) are the dynamical conditions and the last one is a kinematic condition.

When a partially wetting liquid drop stays on a solid surface, the interface intersects with the flat surface and they form a contact angle (θ). In the absence of external force, surface forces acting at the contact line are given by the well-known Young's equation

$$\sigma_{sg} = \sigma_{sl} + \sigma\cos\theta_0, \tag{2.4}$$

when there is no motion. Here θ_0 is the static equilibrium contact angle. σ_{sg}, σ_{sl}, and σ are the surface tension coefficients between solid-gas, solid-liquid, and gas-liquid phases, respectively. In the presence of a shear flow, the liquid-gas interface of the drop normally deforms and the contact angles at the front (advancing) and at the back (receding) of the drop may differ from the static equilibrium contact angle (θ_0). Determination of the dynamic equilibrium contact angle θ_d that occurs when the drop moves on a solid surface is the subject of much theoretical and experimental research. Equation (2.4) has to be modified when the contact line moves due to the well-known contact angle hysteresis. Dussan V. [4] derived a relationship between the speed (U) of the contact line and the dynamic contact angle θ_d,

$$\theta_d - \theta_0 = H(U), \tag{2.5}$$

with $H(\cdot)$ being a function that is determined by experiments. Linear functions are most common but non-linear ones also have been used by Brochard-Wyart and Gennes in [2].

In addition, the no-slip boundary condition leads to the unrealistic prediction of unbounded stresses and viscous dissipation at the contact line. To avoid a non-integrable singularity, the no-slip condition can be replaced with the Navier slip condition

$$v_\tau = \frac{1}{\beta}\frac{\partial v_\tau}{\partial n}, \tag{2.6}$$

where $v_\tau = \vec{v}\cdot\vec{\tau}$ is the velocity component tangential to the surface and β is the slip coefficient. The slip condition has been used in the previous work on the liquid spreading (see, Dussan V [3], Hocking [8] and Leger & Joanny [10]).

3. Numerical Method

3.1. A front-tracking method. To solve the problem stated in the previous section, we use the front-tracking method and follow the approach used in [20, 21]. We reformulate the problem as follows. First of all, the Navier-Stokes equations are modified as

$$\frac{\partial \rho\vec{v}}{\partial t} + \nabla\cdot(\rho\vec{v}\vec{v}) = -\nabla p + \vec{g} + \nabla\cdot(2\mu D) + \int_\Gamma \sigma\kappa\vec{n}\delta\left(\vec{x}-\vec{X}\right)ds, \tag{3.1}$$

where $\delta\left(\vec{x}-\vec{X}\right)$ is a two-dimensional Dirac-delta function and the integral is along the interface Γ. The viscosity and the density are now piecewise constant functions with a jump at the interface. Compared to the original Navier-Stokes equations, (3.1) has an extra singular term which accounts for the forces at interface. Because of the nature of the delta function, (3.1) is the same as the original Navier-Stokes equations (2.1) away from the interface. On the interface, it can be shown that (3.1) is equivalent to the first two conditions of (2.3). As the Dirac-delta function has a finite support, the integral along the interface for every point in the flow is practically only on a small part of it. This technique was first used by Peskin [12] and the advantage of using (3.1) is that it can be applied to the entire domain including the interface, even if the density ρ and the viscosity μ change discontinuously.

To solve (3.1), we need to know the location of the interface, which can be tracked by using the last condition in (2.3)

$$\frac{d\vec{X}}{dt} = \vec{v}\left(\vec{X},t\right), \text{ on } \Gamma, \tag{3.2}$$

starting from a given initial position of the interface.

Once we know the interface location, we will update the distributions of the density $\rho(\vec{x},t)$ and the viscosity $\mu(\vec{x},t)$. We can introduce an indicator function $I(\vec{x},t)$ (the Heaviside step function) such that its value is zero outside the drop and one inside the drop. This indicator function can be viewed as the solution of the following Poisson equation

$$\nabla^2 I = -\nabla \cdot \vec{G} \tag{3.3}$$

with proper boundary conditions. Here the right side vector function

$$\vec{G} = \int_\Gamma \delta\left(\vec{x} - \vec{X}\right) \vec{n} ds \tag{3.4}$$

is an integral of the two-dimensional Dirac-delta function along the interface. Equation (3.3) can be solved by using standard numerical methods, such as the finite difference method. We will follow the method used in [20, 21] and more details can be found in Section 3.3.

Using the indicator function, density and viscosity of the fluid (inside and outside the drop) can be represented as

$$\begin{aligned}\rho(\vec{x},t) &= \rho_g + (\rho_l - \rho_g) I(\vec{x},t),\\ \mu(\vec{x},t) &= \mu_g + (\mu_l - \mu_g) I(\vec{x},t).\end{aligned}$$

Another useful identity concerning the tracking of the interface (3.2) is

$$\vec{v}(\vec{X},t) = \int \vec{v}(\vec{x},t)\delta\left(\vec{x} - \vec{X}\right) d\vec{x}, \tag{3.5}$$

which can be used to obtain the average velocity at $\vec{X}$ point by further using the discrete Dirac-delta function. The integral on the right hand side can be evaluated by averaging over a small area around the interface.

3.2. Boundary conditions. It is well-known that the standard no-slip condition for the velocity leads to a non-integrable singularity in stress at the moving contact line. Various models have been proposed to resolve this singularity [3, 8, 10, 18, 19]. Among them, Dussan V [3], Hocking [8] introduced a model which produces a slip-velocity at the contact line, similar to the Navier slip condition (2.6). The slip coefficient β is determined by a measure of surface roughness. Shikhmurzaev [18, 19] used matching asymptotic expansions to analyze the moving contact line in great detail from hydrodynamics point of view. In this study we use the slip condition (2.6). The velocity component tangential to the solid surface, $v_\tau = \vec{v} \cdot \vec{\tau}$, is given by

$$\frac{\partial v_\tau}{\partial n} = \beta v_\tau. \tag{3.6}$$

For the static drop on the solid surface, the static equilibrium contact angle θ_0 is obtained by Young's equation (2.4). When the liquid drop moves on the surface, the contact angle θ will differ from θ_0 until an equilibrium is established. At the equilibrium, the advancing contact angle at the front of the drop θ_a is greater than θ_0; and at the back of the drop the receding contact angle θ_r is smaller than θ_0 (see Figure 3.1).

(a) (b)

FIG. 3.1. *Sketch of (a) a static drop on a solid surface and (b) a moving drop on a solid surface.*

Let θ_d represent the dynamic equilibrium contact angle at the contact line, it satisfies the following equation (see, Brochard-Wyart & Gennes [2], Shanahan & Carre [17])

$$F_s = \sigma_{sg} - \sigma_{sl} - \sigma \cos\theta_d, \tag{3.7}$$

where F_s is the friction force at the contact line. Using Einstein's equation, the force F_s and the slip velocity v_τ of the drop at the contact line have the following relationship (see, [14])

$$v_\tau = \frac{d}{kTan_L} F_s, \tag{3.8}$$

where d is the surface diffusion coefficient with $d = \frac{\delta}{2} \nu e^{-E/kT}$, and δ is the distance between two successive potential wells located on the solid surface, ν is the vibration frequency of a molecule in the potential well; k is the Boltzmann constant, E is an activation energy, T is the absolute temperature; n_L is the number of the molecules of liquid per unit volume of liquid; and a is the volume of the liquid per unit area of the solid surface. Applying the Young's equation (2.4), equation (3.7) and equation (3.8) lead to that

$$\frac{kTan_L}{d} U = \sigma (\cos\theta_0 - \cos\theta_d), \tag{3.9}$$

where U $(:= v_\tau)$ is the contact line speed. When θ_d is close to θ_0 and θ_0 is not small, (3.9) can be further simplified as

$$\theta_d - \theta_0 = C_f U. \tag{3.10}$$

where $C_f = kTan_L / d\sigma \sin\theta_0$ is called the friction parameter here. We note that other approaches were used in [2, 4, 14] where similar versions of (3.10) were derived using energy arguments. Another model is used for nanometric deformations on soft substrates recently in [17] where a general form of (2.5) is given.

3.3. Discretization. We are now ready to discuss the numerical scheme in more detail. First we set up a staggered grid with grid size h to cover the computation domain. The pressure p and indicator function I are defined at the center of each rectangle, the values of the horizontal velocity are defined at the midpoints of the vertical sides, and the values of the vertical velocity are defined at the midpoints of the horizontal sides. The marker mesh for the interface is a fine grid with a small step size. We start by assuming that the drop is at rest and the position and shape of the drop are known. And we solve the problem by marching in time.

Following Peskin [12] (see also [21]), the delta function is regularized as a distribution function with a compact support

$$\delta_h\left(\vec{x}-\vec{X}\right)=\begin{cases}(4h)^{-\alpha}\Pi_{i=1}^{\alpha}\left(1+\cos\frac{\pi}{2h}(x_i-X_i)\right), & |x_i-X_i|<2h, i=1,\alpha;\\ 0, & \text{otherwise}\end{cases} \tag{3.11}$$

where α is the number of dimensions. Essentially, the sharp interface is now replaced by a transition layer with a thickness $4h$. The interface corresponds to a level set of the indicator function represented by a set of markers $\{\vec{X}^{(l)}\}$. The indicator function is solved by a discrete version of (3.3) with a discretization of (3.4) as

$$\vec{G}(\vec{x})=\sum_l \delta_h\left(\vec{x}-\vec{X}^{(l)}\right)\vec{n}^{(l)}\Delta s^{(l)} \tag{3.12}$$

where $\Delta s^{(l)}$ is the arc-length of the interface (or distance) between two markers $\vec{X}^{(l-1)}$ and $\vec{X}^{(l)}$. The values of the physical parameters, i.e., ρ and μ are updated using the indicator function.

The forcing term from the interface in the Navier-Stokes equations is discretized by using the discrete Delta function as follows

$$\vec{F}(\vec{x})=\sum_l \delta_h\left(\vec{x}-\vec{X}^{(l)}\right)\vec{f}^{(l)}+\sum_c \delta_h\left(\vec{x}-\vec{X}^{(c)}\right)\vec{f}^{(c)}, \tag{3.13}$$

where

$$\vec{f}^{(l)}=\sigma\kappa^{(l)}\vec{n}^{(l)}\Delta s^{(l)}. \tag{3.14}$$

acts at the marker point $\vec{X}^{(l)}$ on the interface Γ, $\vec{f}^{(c)}$ acts on the contact line $\vec{X}^{(c)}$ and restores the contact angle to $\theta_d=\theta_0+H(U)$.

During the dynamic process, the contact angle θ at the moving contact line changes until it equals the dynamic equilibrium contact angle θ_d. Similar as equation (3.7), the force acting on the contact line is given as

$$\vec{f}^{(c)}\cdot\vec{\tau}=\sigma\cos\theta-(\sigma_{sg}-\sigma_{sl}-F_s). \tag{3.15}$$

When θ reaches θ_d, it holds the dynamic equilibrium equation (3.7) and thus $\vec{f}^{(c)}\cdot\vec{\tau}=0$. Using Young's equation (2.4), equation (3.7) and (2.5), the force at the moving contact line can be further derived as

$$\vec{f}^{(c)}\cdot\vec{\tau}=\sigma\left[\cos\theta-\cos\left(\theta_0+H(U)\right)\right], \tag{3.16}$$

at the contact line, where θ is the moving contact angle. The linear formulation for $H(U)$ is $H(U)=C_fU$ which is derived in equation (3.10). In order to obtain the average velocities U at the contact line, we use the identity relation (3.5) combining the discrete delta function

$$U = \sum_{i,j} u_{i,j} \delta_h \left(\vec{x}_{i,j} - \vec{X}^{(c)} \right), \tag{3.17}$$

and apply the extension of the horizontal velocity component $u(\vec{x},t)$ based on the Navier-slip boundary condition (2.6). As the sharp interface is replaced by a layer, $\vec{F}$ is non-zero inside the layer. The Navier-Stokes equations can now be solved using the Marker and Cell (MAC) approach on the staggered mesh, i.e., the velocity is computed using (3.1) and pressure is solved using a Poisson equation derived from (3.1) and the divergence-free constraint (2.2).

Once the values of velocity and pressure are obtained, we calculate the velocity of the interface, indicated by a level set of the indicator function, using the discrete version of (3.5) with the delta function again replaced by (3.11). The new location of the markers on the interface is computed using (3.2). In addition, in order to maintain accuracy, we use a clamped cubic spline to fit the interface using the new marker location and a new set of markers is chosen based on the splines. The cubic spline is also used to compute the curvature of the interface, which thus maintains the accuracy of the approximation curvature.

Let Δt be the time step size, $\Delta t = T/N$, where T is the time period and N is an integer number. The algorithm can be described as follows:

```
Algorithm:
 Step 1. Initialization: $n = 0$
         Input the initial velocity and the marker points of the initial interface.
 Step 2. for $n = 1,2,\ldots,N$ do
         Step 3. Compute indicator function by solving (3.3), and define the distributions of the density and viscosity.
         Step 4. Compute pressure using a Poisson equation derived from the Navier-Stokes equation (3.1) and the divergence-free constraint (2.2).
         Step 5. Compute velocity from the Navier-Stokes equation (3.1) with the slip-condition (2.6) and the force term (3.13) on the staggered mesh.
         Step 6. Calculate the new interface using (3.2) and the cubic spline method. Calculate the curvature of the interface.
         end do
```

Remark 3.1. *The MAC type of staggered grid formulation is chosen here so that the incompressibility condition can be strictly enforced away from the interface. We note that in Peskin's original formulation of the immersed boundary method, incompressibility is not strictly preserved at the interface. In other words, the drop/bubble may "lose its mass" during the computation. This could be a problem if computations are carried out over a long period of time. To handle the incompressibility better, one can either use the immersed interface method [11] or the improved version of the immersed boundary method.*

4. Numerical Experiments

To illustrate the numerical method proposed in this study, we present three numerical examples and grid refinement tests in this section. In the first example,

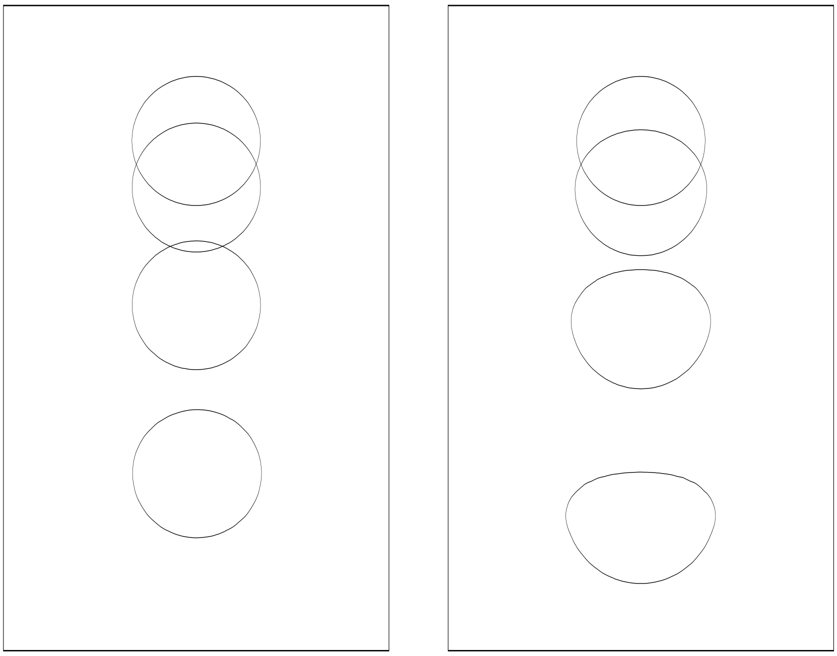

(a) (b)

FIG. 4.1. *Falling drop due to gravity at* $t=0$, 0.1, 0.2, *and* 0.3. *(a)* $E_o=0.0025$*; (b)* $E_o=2{,}500$.

a circular drop (fluid inside the circle is heavier and more viscous than that outside the circle) is initially placed in the middle of the computation domain. At $t>0$, gravity force is applied and the velocity of the fluid at the boundary of the domain is maintained as zero. In the second and third examples, we consider the motion of a two dimensional liquid drop (or a gas bubble) with a given volume $\Omega=(0:1)\times(0:1)$ on a flat solid surface. At $t=0$ the drop (or bubble) is resting on the solid surface with the fluid outside the drop also at rest. At time $t>0$, the outside fluid (air) starts moving, driven by a shear flow parallel to the flat surface. The examples focus on investigating the behaviour of moving drops and bubbles on a solid surface under the influence of flow conditions of the external fluid and the wetting properties of the flat solid surface. The second example considers the motion of the bubble (fluid inside the circle is lighter and less viscous than that outside the circle) on the left boundary and an upward uniform velocity is applied at the right boundary at $t>0$. In the third test, we replace the bubble in the second example by a drop and compute the motion of the liquid drop on a solid surface. Finally, we show that the computations are grid-independent by taking grid refinement tests.

Example 4.1. In this test, we consider the motion of a liquid drop falling in a two dimensional domain due to gravity $g=9.8$. The diameter of the liquid drop is set to be $d_e=0.1$. The boundary conditions are given as

$$u(0,y,t)=u(1,y,t)=u(x,0,t)=u(x,1,t)=0,$$

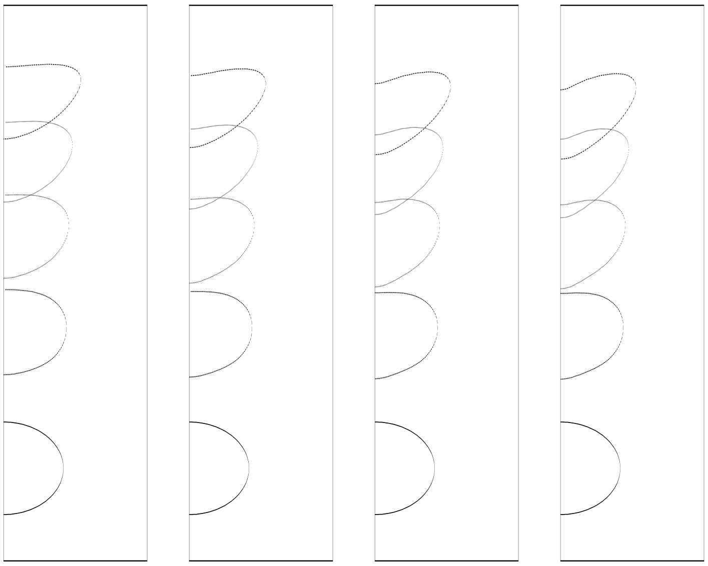

(a) $C_f = 0.5$ (b) $C_f = 1$ (c) $C_f = 1.5$ (d) $C_f = 2$

FIG. 4.2. *Motion of a bubble on a solid surface under shear at* $t = 0$, 0.2, 0.4, 0.6 *and* 0.8. *Vary the friction parameter* C_f *from* 0.5 *to* 2. *Other data are fixed as* $\theta_0 = \pi/2$, $\sigma = 0.001$, $M_\rho = 40$, $M_\mu = 40$, $d_e = 0.1$, $\beta = 0.03$, *and* $V_b = 2$.

and

$$v(0,y,t) = v(1,y,t) = v(x,0,t) = v(x,1,t) = 0.$$

The initial conditions are $u(x,y,0) = v(x,y,0) = 0$. The density and viscosity ratios $\rho_i/\rho_o = \mu_i/\mu_o = 40$, where subscripts o and i stand for values outside and inside the drop, respectively. In addition, we set $\rho_i = 1.0$ and $\mu_i = 0.01$. The surface tension σ is varied as it determines the shape of the interface separating the two fluids. More precisely, we use a non-dimensional parameter called the Eotvos number (or Bond number) $E_o = \rho_o g d_e^2/\sigma$, which is the ratio of the gravity and the surface tension force. The main purpose of this example is to test our method before the simulations for more complicated cases are carried out.

Figure 4.1(a) is the evolution of the interface which separates the two fluids at $t = 0$, $t = 0.1$, $t = 0.2$ and $t = 0.3$ with $E_o = 0.0025$ while the shape of the falling drop with $E_o = 2{,}500$ at the same time intervals is shown in Figure 4.1(b). It can be seen that the shape of the drop is clearly affected by the value of the Eotvos number (or Bond number). The shape of the liquid drop remains circular when the Eotvos number is small (corresponding to a large surface tension coefficient). When the Eotvos number is large (corresponding to a small surface tension coefficient), however, significant deformation can be observed. In another words, the surface tension coefficient affects the shape of the drop. This is consistent with experimental observations.

Example 4.2. We consider the motion of a bubble attached to the left boundary (a solid surface) under a shear flow parallel to the solid surface. Since *ad hoc* models are used to compute the moving contact line and dynamic contact angle, it is necessary to address the effect of the slip parameters β, static contact angle θ_0, friction parameter C_f on the motion of the bubble. Meanwhile, we also consider the impact of the value of the shear velocity. In this example, the boundary conditions are given as

$$u(0,y,t)=u(1,y,t)=u(x,0,t)=u(x,1,t)=0,$$

$$\partial v/\partial x(0,y,t)=\beta v(0,y,t),\quad v(1,y,t)=V_b,\quad v(x,0,t)=v(x,1,t)=V_b x,$$

with a given shear velocity $V_b>0$. The initial conditions are $u(x,y,0)=v(x,y,0)=0$. No gravity force is applied. And we choose the density of outside liquid $\rho_o=1.0$ and the viscosity of outside liquid $\mu_o=0.01$, and let $M_\rho=\rho_o/\rho_i>1$, $M_\mu=\mu_o/\mu_i>1$ denote the ratios of the densities and viscosities of the two liquids, respectively.

First, we investigate the effect of the friction parameter C_f to the motion of the bubble. We change C_f from $C_f=0.5$ to $C_f=2.0$. The diameter of the initial gas bubble is set to be $d_e=0.1$. Other parameters are chosen as the surface tension coefficient $\sigma=0.001$, the ratio of densities $M_\rho=40$, the ratio of viscosities $M_\mu=40$, the slip coefficient $\beta=0.03$, the static contact angle $\theta_0=\pi/2$, and the shear velocity $V_b=2$. The Weber number is defined as $W_e=\rho_o v^2 d_e/\sigma$, which is usually used to characterize the bubble (or drop). In this case, $W_e=400$. The numerical results of the motion of the bubble are given in Figure 4.2 at $t=0, t=0.2, t=0.4, t=0.6$, and $t=0.8$. We can see the impact of the friction parameter C_f on the shape of the bubble while the initial shape of the bubble is a half circle at $t=0$. It is clear in Figure 4.2 that the shapes of the bubble are changed as the time increases and the advanced contact angle becomes bigger than the static one $\theta_0=\pi/2$ but the backward contact angle gets smaller than it at $t=0.4, 0.6$ and 0.8. Moreover, the increasing of the friction parameter C_f from $C_f=0.5$ to $C_f=2.0$ will increase the advanced contact angle and decease the backward contact angle as shown in Figure 4.2(b)-(d).

Now we study numerically the impact of the slip coefficient β by choosing four values $\beta=0.03$, 0.3, 1 and 3 with a static contact angle $\theta_0=2\pi/3$. We compute the motion of the bubble with the following data. The diameter of the gas bubble is $d_e=0.08$, The friction parameter is $C_f=0.5$, and the surface tension coefficient $\sigma=0.001$, the ratio of densities $M_\rho=40$, the ratio of viscosities $M_\mu=40$ and the shear velocity along the right boundary $V_b=2$. The numerical results of the effect of the slip coefficient β are given in Figure 4.3 at $t=0$, 0.2, 0.4, 0.6, and 0.8. The bubble is allowed to slip more easily when β is small Figure 4.3(a). A bigger value of β clearly makes it difficult for the bubble to slide along the surface, indicated by the less distance travelled by the bubble as shown in Figure 4.3(d). It also can be seen that the deformation is more visible and the dynamic contact angles are affected by the slip coefficient β in Figure 4.3(b)-(d).

In Figure 4.4, the shape and the motion of the bubble are shown though different static contact angles θ_0: (a). $\theta_0=\pi/6$ and $d_e=0.36$; (b). $\theta_0=\pi/3$, and $d_e=0.16$; (c). $\theta_0=\pi/2$, $d_e=0.1$; (d). $\theta_0=2\pi/3$ and $d_e=0.08$. Other parameters are chosen as $\beta=0.03$, $\sigma=0.001$, $C_f=0.5$. $M_\rho=40$, and $M_\mu=40$. The shear velocity is chosen as $V_b=2.0$. The effect of the static angle is clear to the shape of the bubble and the dynamic contact angles. In Figure 4.4(a) with the static contact angle $\theta_0=\pi/6$, we can see that the advanced angle becomes bigger than $\pi/6$ while the backward contact angle becomes less than $\pi/6$. For the case with $\theta_0=\pi/3$ in Figure 4.4(b), the advanced contact angle is bigger than $\pi/3$ while the backward contact angle is less that $\pi/3$. Similar results are shown for the cases with $\theta_0=\pi/2$ and $\theta_0=2\pi/3$ in Figure 4.4(c)-(d). Thus, it is clear that the advanced dynamic angle would be

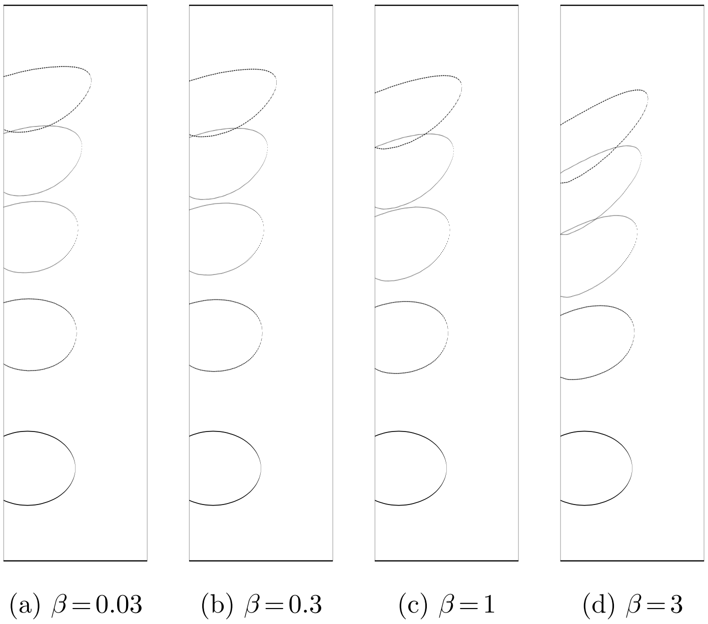
(a) $\beta = 0.03$ (b) $\beta = 0.3$ (c) $\beta = 1$ (d) $\beta = 3$

FIG. 4.3. *Motion of a bubble on a solid surface under shear at* $t = 0$, 0.2, 0.4, 0.6, *and* 0.8. *Change slip coefficient* β *from* 0.03 *to* 3. *Other parameters are chosen as* $\theta_0 = 2\pi/3$, $C_f = 0.5$, $\sigma = 0.001$, $M_\rho = 40$, $M_\mu = 40$, $d_e = 0.08$, *and* $V_b = 2$.

larger than the static contact angle when the bubble moves, however, the backward dynamic angle would normally be smaller than the static one. This has been shown in experimental researches.

To investigate the effect of shear velocity V_b along the right boundary, the shapes of the bubble are given in Figure 4.5 at $t = 0$, 0.2, 0.4, 0.6 and 0.8. The data are chosen as $\beta = 0.03$, $C_f = 1.0$, $\sigma = 0.001$, and $M_\rho = 40$ and $M_\mu = 40$. The diameter of the bubble is $d_e = 0.1$ and the static contact angle is $\theta_0 = \pi/2$. Vary the shear velocity V_b from $V_b = 1$ to $V_b = 2.5$. The larger shear velocity causes the bubble to move faster than that with a smaller applied shear velocity as shown in Figure 4.5. And it can also be seen that the dynamic contact angle is affected by the value of the applied shear velocity.

Example 4.3. We now consider the motion of a drop attached to the left boundary (a solid surface) under a shear flow parallel to the solid surface. The boundary conditions are given as in Example 4.2. The ratios of the densities and viscosities are defined as $M_\rho = \rho_i/\rho_o$ and $M_\mu = \mu_i/\mu_o$, respectively. The density of the inside liquid is chosen as $\rho_i = 1.0$ and the viscosity of the inside liquid is chosen as $\mu_i = 0.01$. The diameter of the drop is given as $d_e = 0.1$. No gravity force is applied.

In Figure 4.6, the shape of the drop is shown at $t = 0, t = 0.2, t = 0.4, t = 0.6$, and $t = 0.8$ for the following cases.

(a) $\sigma = 10^{-6}$, $M_\rho = 40$, $M_\mu = 40$, $\theta_0 = \pi/2$, $\beta = 5$, $C_f = 10$, and $V_b = 2$;
(b) $\sigma = 10^{-6}$, $M_\rho = 40$, $M_\mu = 40$, $\theta_0 = \pi/2$, $\beta = 5$, $C_f = 10$, and $V_b = 3$;
(c) $\sigma = 10^{-6}$, $M_\rho = 20$, $M_\mu = 20$, $\theta_0 = \pi/2$, $\beta = 0.5$, $C_f = 10$, and $V_b = 2$;
(d) $\sigma = 10^{-6}$, $M_\rho = 20$, $M_\mu = 20$, $\theta_0 = \pi/2$, $\beta = 5$, $C_f = 10$, and $V_b = 2$;

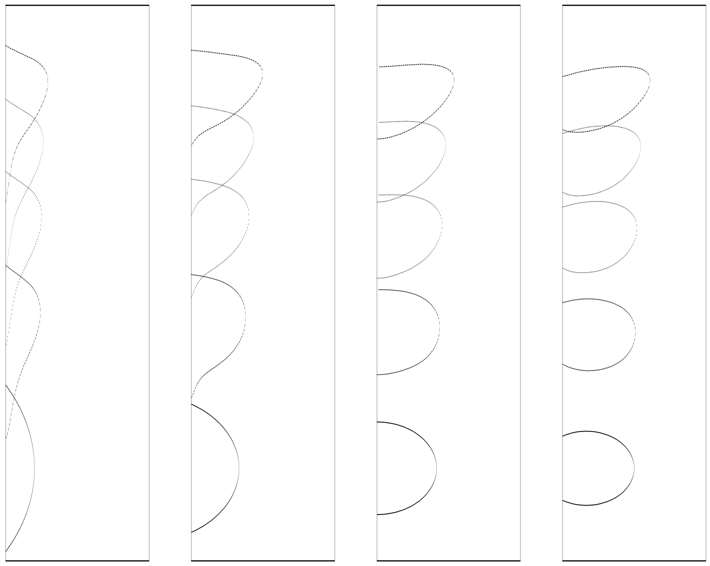

(a) $\theta_0 = \pi/6$ (b) $\theta_0 = \pi/3$ (c) $\theta_0 = \pi/2$ (d) $\theta_0 = 2\pi/3$

FIG. 4.4. *Shape of a bubble on a solid surface under shear at* $t = 0$, 0.2, 0.4, 0.6 *and* 0.8. *Consider the effect of the static contact angle* θ_0. *The data are given as* $\beta = 0.03$, $C_f = 0.5$, $\sigma = 0.001$, $M_\rho = 40$, *and* $M_\mu = 40$. *The shear velocity* $V_b = 2.0$. *The static angle and the diameter of the bubble are chosen as: (a).* $\theta_0 = \pi/6$, $d_e = 0.36$; *(b).* $\theta_0 = \pi/3$, $d_e = 0.16$; *(c).* $\theta_0 = \pi/2$, $d_e = 0.1$; *(d).* $\theta_0 = 2\pi/3$, $d_e = 0.08$.

Figure 4.6(a) shows the motion of the drop with the shear flow $V_b = 2$ at $t = 0, t = 0.2, t = 0.6$ and $t = 0.8$. Figure 4.6(b) shows the shape of the drop with $v_b = 3$ at the same time period. We can see that the drop pushed by a large shear velocity in Figure 4.6(b) moves faster than that in Figure 4.6(a) by applied small shear flow. And it is clear that the advanced dynamic angle in Figure 4.6(b) is bigger than that in Figure 4.6(a) while the backward dynamic contact angle in case (b) is smaller than that in case (a). We compute the motion of the drop with different ratios of $M_\rho = M_\mu = 40$ and $M_\rho = M_\mu = 20$ in Figure 4.6(a),(d). The densities of outside liquids are $\rho_o = 0.025$ in case (a) and $\rho_o = 0.05$ in case (d), the associated Weber number in case (d) is two times than that in case (a). The shape of the bubble in Figure 4.6d with bigger Weber number is much easier to be changed than that in Figure 4.6(a) with smaller Weber number. Meanwhile, the speed of the motion of the drop is clearly affected by the value of the Weber number. Figure 4.6(c),(d) shows the effect of different β, with $\beta = 0.5$ in case (c) and $\beta = 5$ in case (d). It is obvious that the motion of the drop in Figure 4.6(c) is faster than the one in Figure 4.6(d) due to a small β value. And the shape of the drop is also affected by the value of β, as shown in Figure 4.6(c),(d).

If we consider the case with the ratios $M_\rho = 10$ and $M_\mu = 10$ but with the density and the viscosity of outside liquid $\rho_o = 0.1$ $\mu_o = 0.001$. The liquid inside the drop has high density $\rho_i = 1.0$ and high viscosity $\mu_i = 0.01$. In Figure 4.7 we compute the motion of the drop by choosing different β values from $\beta = 0.03$ to $\beta = 15$. Other data are chosen $d_e = 0.1$, $\theta_0 = \pi/2$, $\sigma = 0.0001$, $C_f = 0.5$ and $V_b = 2$. In this case the Weber

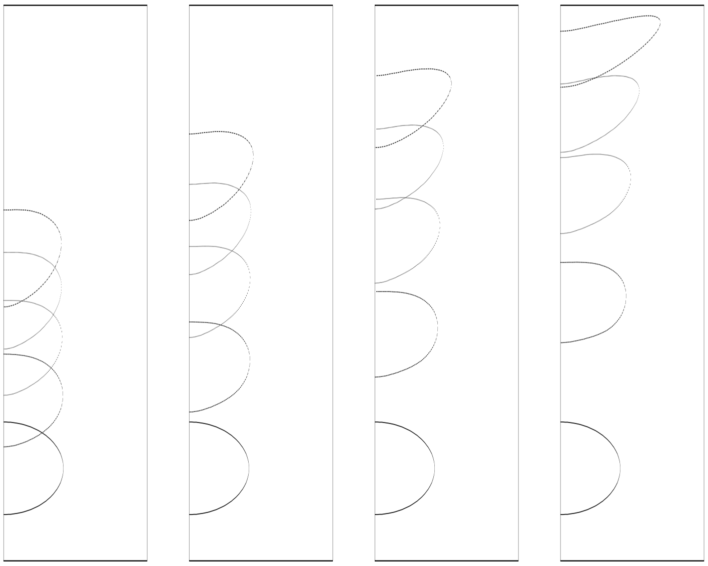

(a) $V_b = 1$ (b) $V_b = 1.5$ (c) $V_b = 2$ (d) $V_b = 2.5$

Fig. 4.5. *Shape of a bubble on a solid surface under shear at* $t = 0$, 0.2, 0.4, 0.6 *and* 0.8. *Apply different shear velocities from* $V_b = 1$ *to* $V_b = 2.5$. *Other data are* $\theta_0 = \pi/2$, $\beta = 0.03$, $C_f = 1.0$, $\sigma = 0.001$, $M_\rho = 40$, $M_\mu = 40$ *and* $d_e = 0.1$.

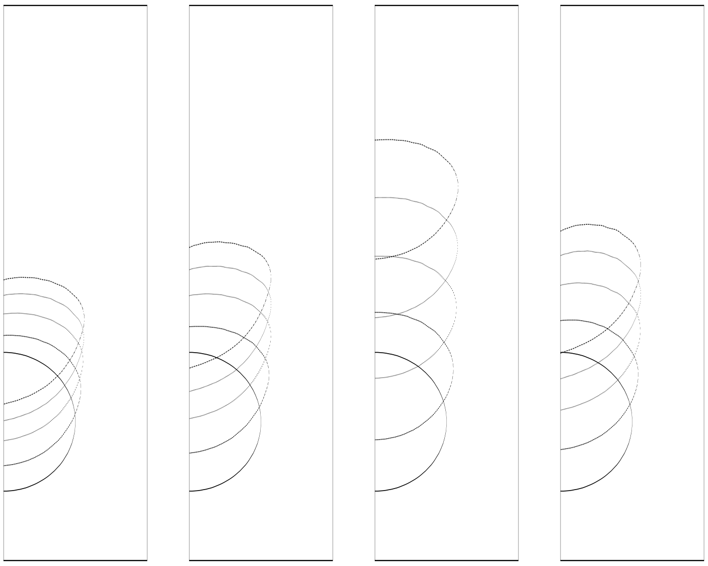

(a) (b) (c) (d)

Fig. 4.6. *Motion of a liquid drop on a solid surface under shear at* $t = 0$, 0.2, 0.4, 0.6 *and* 0.8. *The data are* $\sigma = 10^{-6}$, $C_f = 10$, $\theta_0 = \pi/2$. *Other parameters are (a)* $\beta = 5$, $M_\rho = M_\mu = 40$, $V_b = 2$; *(b)* $\beta = 5$, $M_\rho = M_\mu = 40$, $V_b = 3$; *(c)* $\beta = 0.5$, $M_\rho = M_\mu = 20$, $V_b = 2$; *(d)* $\beta = 5$, $M_\rho = M_\mu = 20$, $V_b = 2$.

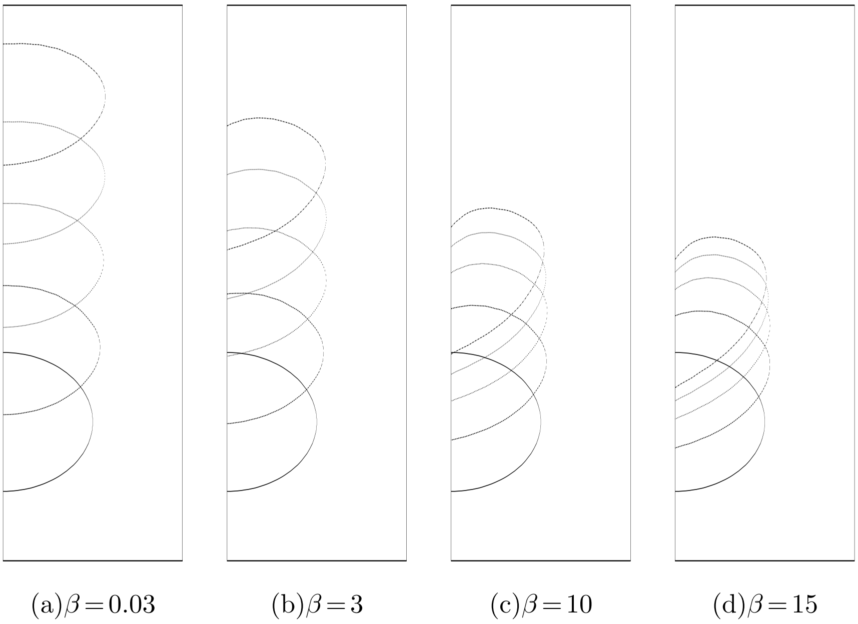

FIG. 4.7. *Motion of a liquid drop on a solid surface under shear at* $t = 0, 0.2, 0.4, 0.6$ *and* 0.8. *Vary the slip coefficient* β *from* $\beta = 0.03$ *to* $\beta = 15$. *Other parameters are determined as* $d_e = 0.1$, $\theta_0 = \pi/2$, $\sigma = 0.0001$, $C_f = 0.5$, $M_\rho = 10$, $M_\mu = 10$, *and* $V_b = 2$.

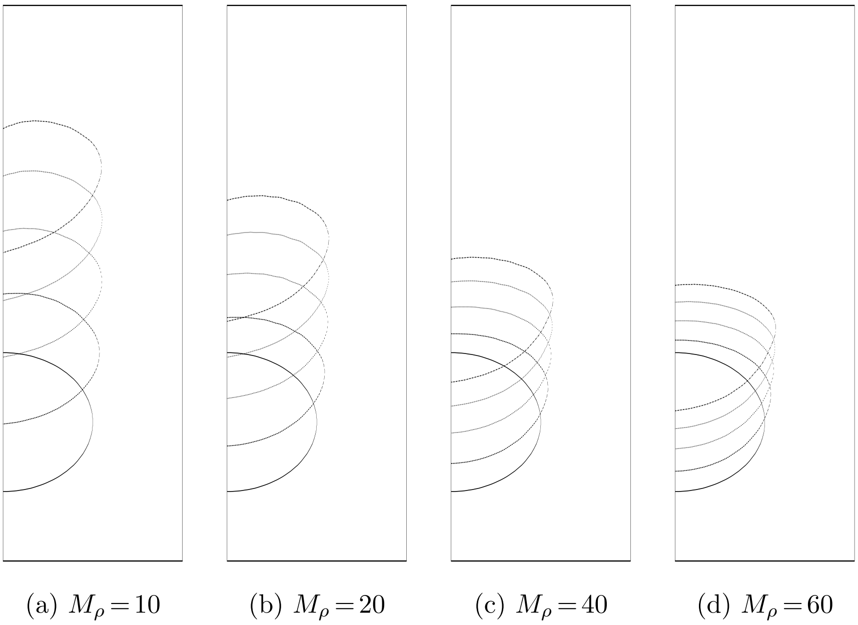

FIG. 4.8. *Motion of a liquid drop on a solid surface under shear at* $t = 0, 0.2, 0.4, 0.6$ *and* 0.8. *Vary the ratios* M_ρ *and* M_μ *of the density and viscosity. Other parameters are determined as* $d_e = 0.1$, $\theta_0 = \pi/2$, $\sigma = 0.00001$, $\beta = 3.0$, $C_f = 1.0$, $V_b = 2$, *and* $M_\mu = M_\rho$.

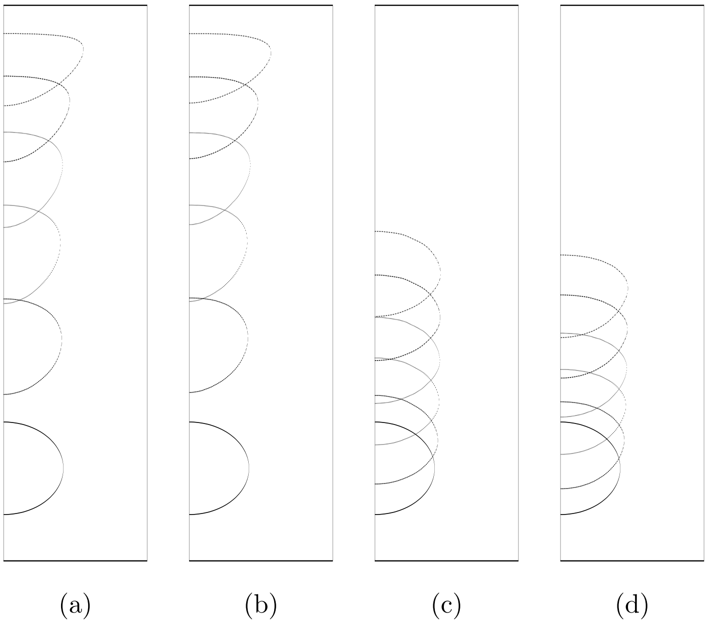

FIG. 4.9. *Grid refinement tests for the motion of a drop (c, d) and a bubble (a, b) at* $t = 0.0, 0.4, 0.8, 1.2, 1.6$ *and* 2.0. *(a, c): use the grid with* $\Delta x = \Delta y = 1/50$. *(b, d): use the refine grid with* $\Delta x = \Delta y = 1/100$.

number is $W_e = 400$. The shape of the drop is clearly to be affected by the value of the slip coefficient β. With the same kind of data $d_e = 0.1$, $\theta_0 = \pi/2$, $\rho_o = 0.1$, $\mu_o = 0.001$ but $\sigma = 0.00001$, $C_f = 1.0$, $\beta = 3.0$, we consider the effect of the ratios of densities and viscosities with the value from $M_\rho = 10$ to $M_\rho = 60$. The shape of the moving drop and speed of the motion of the drop are affected by the ratio values of densities and viscosities, which are shown in Figure 4.8.

Finally, we take the grid refinement tests and show that the computations presented in this paper are grid-independent. Figure 4.9(a) shows the shape of a bubble in Example 4.2 at $t = 0$, $t = 0.4$, $t = 0.8$, $t = 1.2$, $t = 1.6$ and $t = 2.0$, with the diameter $d_e = 0.1$, the surface tension $\sigma = 0.001$, the ratios of the outside and inside liquid densities and outside and inside liquid viscosities $M_\rho = \dfrac{\rho_o}{\rho_i} = 40$ and $M_\mu = \dfrac{\mu_o}{\mu_i} = 40$, the slip coefficient $\beta = 0.03$, the friction parameter $C_f = 0.5$, the static contact angle $\theta_0 = \pi/2$, and the shear velocity $V_b = 1$ along the right boundary, computed using the step sizes $\Delta x = \Delta y = 1/50$. Figure 4.9(b) are the numerical results using a smaller grid sizes $\Delta x = \Delta y = 1/100$. Figure 4.9(c)-(d) shows the effect of the grid refinement on the shape of the drop in the Example 4.3 at $t = 0$, $t = 0.4$, $t = 0.8$, $t = 1.2$, $t = 1.6$ and $t = 2.0$. The data are chosen as $d_e = 0.1$, $\sigma = 10^{-6}$, $\beta = 0.05$, $C_f = 0.05$ and $\theta_0 = \pi/2$, $V_b = 1$. The inside liquid density and viscosity are $\rho_i = 1.0$, $\mu_i = 0.01$, and the ratio of the inside and outside liquid densities $M_\rho = \dfrac{\rho_i}{\rho_o} = 40$, the ratio of the inside and outside liquid viscosities $M_\mu = \dfrac{\mu_i}{\mu_o} = 40$. Figure 4.9(c) is the shape of the drop obtained using the grid sizes $\Delta x = \Delta y = 1/50$. Figure 4.9(d) is the result using a smaller grid sizes $\Delta x = \Delta y = 1/100$. It is clear that the shapes of the bubble and the drop are almost similar, as shown in Figure 4.9.

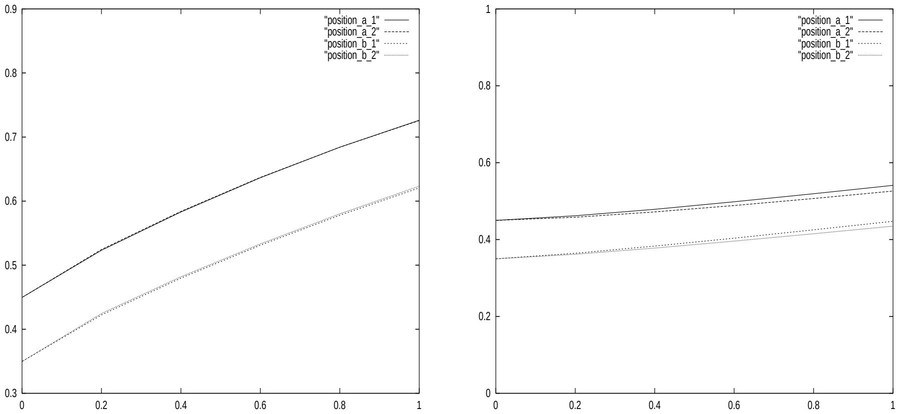

(a) (b)

Fig. 4.10. *Comparison of the positions of moving contact lines on grid refinement tests. (a) The positions of moving advanced and backward contact lines of the bubble. (b) The positions of moving advanced and backward contact lines of the drop.*

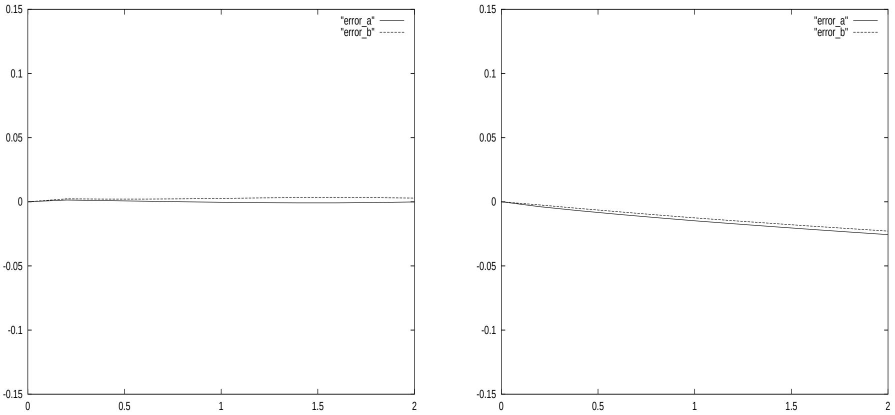

(a) (b)

Fig. 4.11. *The errors of moving contact lines on grid refinement tests. (a) The errors of moving contact lines of the bubble; (b) The errors of moving contact lines of the drop. Where* $error_a$ *is the error at the advance contact line and* $error_b$ *is the error at the back contact line.*

The computed positions of moving contact lines of the bubble and the drop using the grid ($\Delta x = \Delta y = 1/50$) and refined grid ($\Delta x = \Delta y = 1/100$) are shown in Figure 4.10. In Figure 4.10(a) the two upper curves are the moving curves of the advanced contact line of the bubble computed with these two grids. The two lower ones are the moving positions of the backward contact line of the bubble. The Figure 4.10(b) shows the case of the drop. The errors of moving contact lines with these two grids are given in Figure 4.11. Figure 4.11(a) shows the errors of advanced and backward contact lines of the bubble. Figure 4.11(b) gives the contact line errors of the drop.

From Figures 4.9-4.11, we can see that the results are grid-independent.

5. Discussion

In this study, we have developed a front-tracking method to compute the motion of a two-dimensional drop/bubble attached to a plane surface. For the motion of contact line and the determination of the dynamic contact angle, we use *ad hoc* models. The motion of fluids near the contact lines along the solid surface is modelled by a Navier slip condition and the local forces are introduced at the moving contact lines, based on a relationship of moving contact angle and contact line speed. Numerical tests are carried out to investigate the effect of the slip coefficient β, friction parameter C_f and the static contact angle θ_0. It is clear that the values of β, C_f and θ_0 affect the motion and the shape of the interface besides the dynamic contact angles. Grid refinement tests are given to show the computations grid-independent. The method developed in this paper can be applied to the motion of drops and bubbles on a solid surface over a wide range of parameter values.

Ideally we would like to compare our computations with experimental measurements or existing numerical results. However experiments for two dimensional drops were done only for thin strips of silicon oil spreading down a vertical glass plate [6]. The thickness of the strip ($50\mu m$) in the experiments is thin compared with the length ($3mm$ in diameter), thus it falls into the lubrication approximation region. Most of the existing numerical and analytical studies were also done for thin drops or in the limit of creeping flows. Our paper has focused on fat drops/bubbles where lubrication approximation breaks down. Thus a direct comparison with experimental measurements and existing numerical results was not attempted in this paper.

As a next step, a more careful study on the slip velocity model will be conducted near the moving contact lines. Since the no-slip condition is considered a good approximation away from the contact line, it is more reasonable to consider β as a function of the distance from the contact line. It will be interesting to investigate whether a range of β exists in which the motion of the bubble/drop and the shape of the interface is not affected by the value of β. Finally, in order to determine the value (or function) of β and C_f, a more fundamental approach must be employed. To accurately simulate the behavior of the moving bubble near the contact line, local refinement near the contact line and a refined mark point grid for the free surface will be developed. Microscopic approaches may be considered as well. As the direct numerical simulation using molecular dynamics is still beyond the reach of current computing power, approaches using the lattice Boltzmann equation [15] or a diffusive interface model [16] provide two interesting alternatives. Alternatively, results from the molecular dynamics simulations [13] may be incorporated into our numerical method.

Acknowledgement. This research is supported by the natural Sciences and Engineering Research Council (NSERC) of Canada and the Mathematics of Information and Complex Systems (MITACS). The authors thank the referees for their invaluable comments and suggestions which helped improving the paper greatly.

REFERENCES

[1] S. Betelu, J. Diez, L. Thomas, R. Gratton and B. Marino, *A boundary element method for viscous gravity currents*, Int. J. Numer. Meth. Fluids, 25, 1-19, 1997.

[2] F. Brochard-Wyart and P.G. de Gennes, *Dynamics of partial wetting*, Adv. Colloid Interface Sci., 39, 1-11, 1992.

[3] E. B. Dussan V., *The moving contact line: the slip boundary condition*, J. Fluid Mech., 77, 665-684, 1976.

[4] E. B. Dussan V., *On the spreading of liquids on a solid surface: static and dynamic contact lines*, Ann. Rev. Fluid Mech., 11, 371-400, 1979.

[5] P. Ehrhard and S. H. Davis, *Non-isothermal spreading of liquid drops on horizontal plates*, J. Fluid Mech., 229, 365-388, 1991.

[6] A. G. Gonzalez, J. Diez, J. Gomba and R. Gratton, *Spreading of a thin two-dimensional strip of fluid on a vertical plane: experiments and modeling*, preprint, 1-17, 2003.

[7] H. P. Greenspan, *On the motion of a small viscous droplet that wets a surface*, J. Fluid Mech., 84, 125-143, 1978.

[8] L. M. Hocking, *A moving fluid interface on a rough surface*, J. Fluid Mech., 76, 801-817, 1976.

[9] J. K. Hunter, Z. Li and H. Zhao, *Reactive autophobic spreading of drops*, J. Comput. Phys., 63, 42-61, 2002.

[10] L. Leger and J. F. Joanny, *Liquid spreading*, Rep. Prog. Phys., 55, 431-486, 1992.

[11] R. J. LeVeque and Z. Li, *The immersed interface method for Elliptic equations with discontinuous coefficients and singular sources*, SIAM J. Numer. Anal., 31, 1019-1044, 1994.

[12] C. S. Peskin, *The fluid dynamics of heart valves: experimental, theoretical, and computational methods*, Ann. Rev. Fluid Mech., 14, 235-259, 1982.

[13] T. Qian, Wang X-P and P. Sheng, *Molecular scale contact line hydrodynamics of immiscible flows*, Phys. Rev. E, 68, 016306, 2003.

[14] E. Ruckenstein, *The moving contact line of a droplet on a smooth solid*, J. Colloid Interface Sci., 170, 284-286, 1995.

[15] R. Scardovelli and S. Zaleski, *Direct numerical simulation of free-surface and interfacial flow*, Ann. Rev. Fluid Mech., 31, 567-604, 1998.

[16] P. Seppecher, *Moving contact lines in the Cahn-Hilliard theory*, Int. J. Engng. Sci., 34, 977-992, 1996.

[17] M. E. R. Shanahan and A. Carre, *Spreading and dynamics of liquid drops involving nanometric deformations on soft substrates*, Colloids and Surfaces A: Physicochem. Eng. Aspects, 206, 115-123, 2002.

[18] Y. D. Shikhmurzaev, *The moving contact line on a smooth solid surface*, Int. J. Multiphase Flow, 19, 586-610, 1993.

[19] Y. D. Shikhmurzaev, *Dynamic contact angles and flow in vicinity of moving contact line*, AIChE J., 42, 601-612, 1996.

[20] G. Tryggvason, B. Bunner, A. Esmaeeli, D. Juric, N. Al-Rawahi, W. Tauber, J. Han, S. Nas and Y.-J. Jan, *A front-tracking method for the computations of multiphase flow*, J. Comput. Phys., 169, 708-759, 2001.

[21] S. O. Unverdi and G. Tryggvason, *A front-tracking method for viscous, imcompressible, multi-fluid flows*, J. Comput. Phys., 100, 25-37, 1992.